Influence of Fe-N-C Morphologies on the Oxygen Reduction Reaction in Acidic and Alkaline Media

Norhamizah Hazirah Ahmad Junaidi[1], Sue Ying Tan[1], Wai Yin Wong[1*], Kee Shyuan Loh[1], Rahman Saidur[2,5], Thye Foo Choo[3] and Bo Wu[4]

[1]*Fuel Cell Institute, Universiti Kebangsaan Malaysia, 43600 Bangi, Selangor, Malaysia*
[2]*Research Centre for Nano-Materials and Energy Technology, School of Engineering and Technology, Sunway University, Jalan Universiti, Bandar Sunway, 47500 Petaling Jaya, Selangor, Malaysia*
[3]*Malaysian Nuclear Agency, Bangi, 43000 Kajang, Selangor, Malaysia*
[4]*H2Green (Ningbo) New Energy Technology Co., Ltd. 3F, Building 17, Fugang Electronic Commerce Mall, No. 5000 Airport Road, Shiqi Subdistrict, Haishu District, Ningbo City, Zhejiang Province, China*
[5]*School of Engineering, Lancaster University, Lancaster, LA1 4YW, UK*

[*]Corresponding author: waiyin.wong@ukm.edu.my

Abstract

The development of non-noble metal oxygen reduction reaction (ORR) catalysts for fuel cells has been motivated by the high cost and limited supply of noble metals, as well as the desire to improve the performance and durability of this type of energy conversion device. In this study, non-noble Fe-N-C catalyst were synthesized using a zeolitic imidazole framework (ZIF-8), poly(aniline), and 10,10′-dibromo-9,9′-bianthry as precursors to produce Fe-N-C with hollow sphere (HS), amorphous bulky structure (B), and sheet-like thin sheet (N) structure. The Fe-N-C catalyst were analysed in terms of their shape, crystal structure, pore characteristics, and elemental composition. Among all the Fe-N-C catalyst, Fe-N-C_HS had the highest total surface area, followed by Fe-N-C_B and Fe-N-C_N. To evaluate their ORR catalytic activity, a half-cell electrochemical experiment with 0.1 M KOH and 0.1 M $HClO_4$ as the alkaline and acidic electrolytes was conducted. This study revealed that Fe-N-C_HS exhibited the highest onset potential but the Fe-N-C_B has the highest limiting current density in alkaline medium; meanwhile in acidic media, Fe-N-C_HS shows the best ORR performance with the highest onset potential and limiting current. This highly porous Fe-N-C_HS catalyst also demonstrated

active site activation and excellent stability compared to the other samples as well as commercial Pt/C in acidic electrolyte, which suggests its potential for application in proton exchange membrane fuel cells (PEMFCs).

Keywords: Fe-N-C, morphology, oxygen reduction reaction, catalytic activity, catalyst stability.

Graphical Abstract

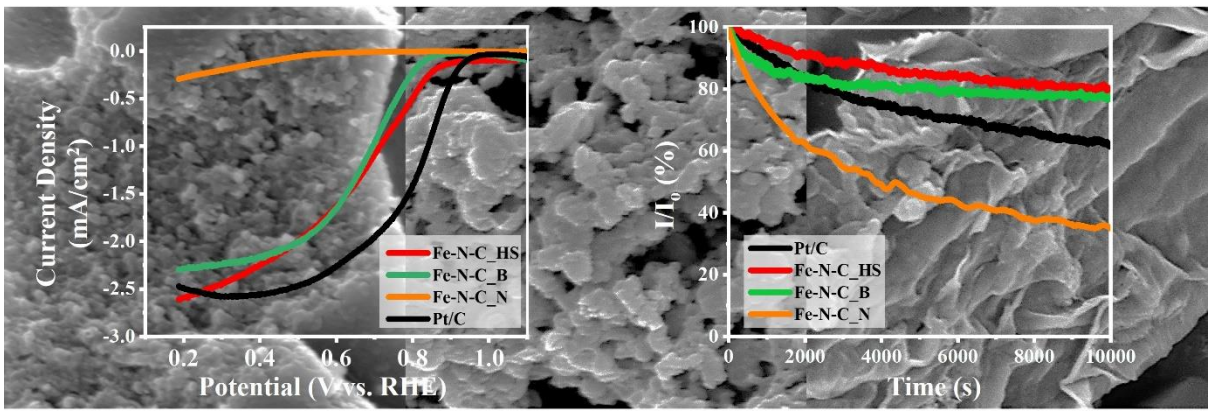

1.0 Introduction

The global introduction of carbon-neutral future has caused fuel cells to be regarded as a future energy generation technology, especially in the automotive industry. By utilizing hydrogen gas as the fuel, fuel cells have been recognized as one of the cleanest energy sources due to their low to no carbon emissions. In fact, the operation of fuel cells produces not only electricity but also water as a byproduct, which is less harmful to the environment. However, the cathodic reaction in fuel cells is the limiting factor that hinders their full utilization due to the multiple electron transfer processes of the oxygen reduction reaction (ORR) that slowing the overall reaction, compared to the hydrogen oxidation reaction (HOR) at the anode which is much faster. To overcome this problem, a platinum group metal (PGM) catalyst was employed as the catalyst to speed up the electrochemical reactions.[1] Despite having high catalytic activity and low overpotential, PGM catalysts are expensive, thus limiting the commercialization of fuel cells in the market.[2] Numerous efforts have been made to find an alternative to expensive PGM-based catalysts, especially by exploring the potential of inexpensive, earth-abundant non-PGM catalysts, such as metal oxides, metal-free catalysts and metal-nitrogen-carbon (M-N-C) catalysts.[3-6] Among the various non-noble metal catalysts, Fe-N-C catalysts have shown great potential as ORR catalysts in fuel cells due to their excellent ORR activity, good stability and low cost. It has been reported through both experimental and simulation work that the electrocatalytic activity of metal-nitrogen-carbon towards the ORR is in the order of Fe > Co > Mn > Cu > Ni.[7,8]

The United States Department of Energy (DOE) has set the goal of developing more cost-effective and efficient PGM electrocatalysts for fuel cells.[9] Various approaches have been applied to find the best Fe-N-C catalyst to achieve the desired performance as required by the DOE, such as controlling the morphology of the catalyst.[10] By controlling the morphology of Fe-N-C electrocatalysts, it is possible to achieve better performance, stability, and mass transport, which can lead to more efficient and durable fuel cells. Recently, the use of metal-organic frameworks (MOFs) as precursors to synthesize Fe-N-C catalysts has increased, owing to their large, ordered porous structures, which allow for more active site exposure and can overcome mass transport issues.[11-13] For example, Lin et al. fabricated a highly porous Fe-N-C through the carbonization of an iron-doped zeolitic imidazolate framework (ZIF-8) on graphene oxide with a total surface area of 1226.2 m^2/g.[14] The fabricated Fe-N-C was reported to exhibit an onset potential of 0.876 V vs. RHE when tested in 0.1 M KOH and a half-wave potential of 0.759 V vs. RHE in 0.1 M $HClO_4$. In addition, the single cell PEMFC performance

was 312 mW/cm^2 when tested under H_2-air conditions. In another study reported by Xu et al., a microwave-assisted Fe-doped ZIF-8 Fe-N-C catalyst with abundant Fe-N_4 sites and pore structures achieved a power density of 61 mW/cm^2 for direct methanol fuel cell testing.[15]

In the last decade, conductive polymers, such as polyaniline (PANI) and polypyrrole (PPy) have been regarded as promising N sources for Fe-N-C. This polymer-derived Fe-N-C catalyst was found to be comparable to the commercial Pt/C catalyst in terms of their ORR activity.[16] In fact, the morphology of the polymer-derived Fe-N-C can be tuned by controlling the nanostructure of PANI through the manipulation of the PANI molecular structure.[17] For instance, He et al. manipulated the PANI molecular structure during the synthesis of Fe-N-C by adjusting the ratio of oxidizing agent to aniline, resulting in different quinoid ring (QR) contents.[18] This is because the higher the degree of oxidation is, the higher the QR content produced. This PANI QR structure is essential for the formation of Fe-N_x active sites during pyrolysis. However, an enormous QR content could lead to the formation of PANI oligomers, which could affect the thermal stability of PANI. The optimum PANI-derived Fe-N-C catalyst from the study was found to exhibit an E_{onset} of 0.89 V vs. RHE with the formation of nanorod-like Fe-N-C when tested in an acidic electrolyte. PANI-containing Fe-N-C is one of the most promising Fe-N-C catalysts with an amorphous, highly disordered porous structure, large surface area and high degree of nitrogen incorporation. These characteristics are beneficial for ORR catalysts in both acidic and alkaline environments.

The ORR proceeds differently in alkaline and acidic media. In acidic conditions, the ORR typically proceeds via an inner-sphere mechanism, where an oxygen molecule directly coordinates with a metal centre in the catalyst.[19] In contrast, in alkaline conditions, the ORR typically proceeds via both inner- and outer-sphere mechanism, where an oxygen molecule coordinates with a water molecule that is adsorbed on the catalyst surface.[19] These different reaction mechanisms lead to different kinetic and thermodynamic parameters, such as the overpotential and product distribution, which ultimately affect the performance of the catalyst in the ORR. In recent years, various methods have been reported for the synthesis of Fe-N-C catalysts, resulting in a range of different morphologies and structures, such as nanoparticles,[20,21] two-dimensional structures,[22] and single atom structures.[23,24] The development of an effective cathode electrocatalyst for fuel cells is crucial to the success of this advanced technology. Generally, nanoarchitecture is an important aspect to consider for electrocatalyst materials in fuel cells.[25,26] However, it remains uncertain whether varying the morphology of Fe-N-C through the use of different precursors affects the catalytic activity and

stability of the ORR catalyst. Our previous work revealed that under alkaline environment, sheet-like structure was able to catalyse the ORR with promising activity.[27,28] However, when tested in an acidic condition, the activity was inferior. Unlike amorphous carbon-based catalyst, despite the lower ORR in acid than in alkaline media, the activity is still promising in acid media. This could be attributed to the difference in catalyst morphology which led to the significant difference in alkaline and acid environment. The intention of this work is to compare the selected morphology of Fe-N-C towards their ORR performance in acid and alkaline media. This work also comprehensively demonstrates the catalyst durability and stability via accelerated durability test (ADT) protocol and chronoamperometry. Therefore, this study focuses on the different morphologies of Fe-N-C catalysts and their effect on ORR activity while also investigating the stability and durability of the catalysts to ensure their practical use in PEMFCs.

2.0 Experimental

2.1 Materials & Synthesis

Zinc nitrate hexahydrate ($Zn(NO_3)_2.6H_2O$), iron (III) nitrate nonahydrate ($Fe(NO_3)_3.9H_2O$), iron (II) phthalocyanine, iron (III) chloride hexahydrate, melamine, 10,10'-dibromo-9,9'-bianthryl monomer, ammonium persulfate, aniline, sodium chloride, methanol and 2-methylimidazole analytical reagent were used without purification. The iron content in the precursors for synthesizing the Fe-N-Cs are fixed for all samples.

Three different Fe-N-C catalysts were synthesized. The first Fe-N-C, (Fe-N-C_HS) was prepared according to the work conducted by Zhang et al. [29] by adding zinc nitrate hexahydrate and iron nitrate nonahydrate into 300 ml of methanol solution at a molar ratio of 1:0.025. Another solution was prepared by adding 2-methylimidazole (1.95 g) in another methanol solution with the same volume. Next, both solutions were mixed together and stirred at 60 °C. After 24 h, the precipitate was collected and washed with ethanol before drying in a vacuum oven at 60 °C. Finally, the catalyst was pyrolyzed at 1,100 °C to ensure the complete removal of the Zn ion.

The second Fe-N-C sample (Fe-N-C_B) was prepared by the polymerization of polyaniline as conducted by Peng et al.,[30] in which aniline (3.33 ml) was added into a mixture of iron chloride hexahydrate (1.25 g), melamine (1.67 g) and 0.75 M hydrochloric acid (100 ml). To complete the polymerization process, ammonium persulfate (8.3 g) as an oxidizing agent was added into the solutions, which were then stirred overnight in an ice bath. Next, the

sample was pyrolyzed at 900 °C for an hour under N_2 flow, followed by acid washing in 0.5 M H_2SO_4 at 80 °C and another pyrolysis reaction under the same conditions.

Finally, the third Fe-N-C sample (Fe-N-C_N) was prepared by applying the template method using NaCl as the work by Chung et al.,[31] in which the precursor, iron phthalocyanine (0.15 g) and 10,10'-dibromo-9,9'-bianthryl monomer (0.85 g) in 100 ml hexane solution were mixed with the NaCl template (150 g) to produce the thin sheet structure. The mixture was stirred at 70 °C and left overnight to allow all the precursors to deposit on the surface of NaCl. Upon evaporation of the solvents, the samples were annealed at 450 °C for an hour under N_2 flow. After that, the NaCl template was removed by washing using deionized (DI) water. The washing process was augmented by using the vacuum filtration method.

2.2 Material Characterization

Field emission scanning electron microscopy (GeminiSEM 500) and transmission electron microscopy (FEI Talos L120C) were used to examine the morphology and structure of the catalysts. X-ray diffraction (XRD) analysis (PANalytical X'Pert PRO) was used to analyse the crystallographic structure of the Fe-N-C catalysts. The percentage of crystallinity (CI) is calculated using the following Equation (1):

$$CI\ (\%) = \frac{A_{cr}}{A_{total}} \times 100 \quad (1)$$

where A_{cr} is the area of the crystalline phase and A_{total} is the total area of the XRD pattern.

X-ray photoelectron spectroscopy (XPS) was performed using a Kratos Axis Ultra with Al Monochromatic to examine the chemical bonding and composition. Nitrogen adsorption-desorption was performed on a Micromeritics 3Flex Analyser at 77 K to obtain information on the surface area and porosity of the Fe-N-C catalyst through the Brunauer-Emmett-Teller (BET) and Barret-Joyner-Halenda (BJH) methods, respectively. The samples were degassed at 150 °C prior to the measurement, with a holding time of 8 hours.

2.3 Electrochemical Measurement

The electrochemical properties of the catalysts were studied using a standard three-electrode cell system. The three-electrode system comprised a glassy carbon rotating ring-disk electrode (GC-RRDE) as the working electrode, an Ag/AgCl electrode with 3 M KCl as the reference electrode and a platinum sheet as the counter electrode. The electrochemical measurements were performed on an Autolab PGSTAT128N potentiostat with 0.1 M KOH and 0.1 M $HClO_4$ as the alkaline and acidic electrolytes, respectively. Catalyst inks were prepared

by dispersing 5 mg of the catalyst with ethanol and 10 wt.% Nafion® solution and sonicated for 30 minutes to obtain a homogeneous mixture of catalyst ink. The GC surface was polished using a 0.05 μm alumina slurry as the polishing liquid until a shiny mirror-like surface was obtained. Next, 10 μl of the catalyst was drop-casted on the GC to obtain a fixed catalyst loading of 0.5 mg cm^{-2}. Finally, the catalyst was allowed to dry at room temperature for an hour before the measurement. All potentials are reported against the reversible hydrogen electrode (RHE) by correcting the potential according to Equation 2.

$$E_{RHE} = E_{Ag/AgCl} + 0.059pH + 0.210 \quad (2)$$

Cyclic voltammetry (CV) was performed at a scan rate of 50 mV/s over a potential window of -0.9 to 0.2 V vs. Ag/AgCl and -0.2 to 0.9 V vs. Ag/AgCl in 0.1 M KOH and 0.1 M $HClO_4$ electrolyte, respectively. Linear sweep voltammetry (LSV) was performed at a scan rate of 10 mV/s over a smaller potential window. All CVs and LSVs were recorded at room temperature. Background capacitive currents in LSV were corrected by subtracting the current in the oxygen-saturated electrolyte from the current in the nitrogen-saturated electrolyte. The same conditions were selected for the commercial Pt/C catalyst (20 wt_{pt}%) with the same catalyst loading as the comparison with the noble metal catalyst.

The electron transfer number (*n*) of the catalysts was calculated using the rotating ring-disk electrode (RRDE) technique. Equation 3 was used for the *n* calculation using the RRDE method, where I_d is the disk current, I_r is the ring current, and *N* is the ring collection efficiency. The percentage of peroxide species produced from the reaction was calculated using Equation 4.

$$n = \frac{4I_d}{I_d + \frac{I_r}{N}} \quad (3)$$

$$HO_2^- \% = \frac{4-n}{2} \times 100 \quad (4)$$

The durability of the Fe-N-C catalyst was evaluated using an accelerated durability test (ADT) according to the ADT protocol from the Department of Energy US (DOE).[32] In a standard ADT protocol, 5000 load cycles were applied at a potential window between -0.3 V and 0.1 V vs. Ag/AgCl in 0.1 M KOH electrolyte and 0.2 and 0.75 V vs. Ag/AgCl in 0.1 M $HClO_4$ electrolyte The ADT tests were performed at room temperature in N_2-saturated electrolyte to investigate the carbon oxidation that occurred during the load cycles.[33] Prior to the ADT testing, CVs and LSVs were recorded as initial measurements.

3.0 Results and discussion

3.1 Analysis of structure and morphology

Figure 1 shows the FESEM analysis of the three Fe-N-C catalysts. As shown in Figure 1 (a, d), the first Fe-N-C had a hollow sphere structure, thus it was labelled as Fe-N-C_HS. However, the particles seemed to agglomerate and form a large hollow structure. Meanwhile, in Figure 1 (b, e), the FESEM image shows that the second Fe-N-C had an irregular bulky structure with a random shape and size, hence it was labelled as Fe-N-C_B. On the other hand, the third Fe-N-C was labelled as Fe-N-C_N, as it exhibited a thin, sheet-like structure (Figure 1 (c, f)). These FESEM images showed that the synthesis method and precursors influenced the structure and morphology of the Fe-N-C catalysts. The elemental mapping from FESEM-EDX, as shown in Figure S1 (Supplementary Information), revealed that the Fe content was fixed at 12.55 wt.% ±0.75 and Fe was distributed uniformly on the surface of the catalysts. The EDX spectrum for all the Fe-N-C catalysts are shown in Figure S2-S4 (Supplementary Information).

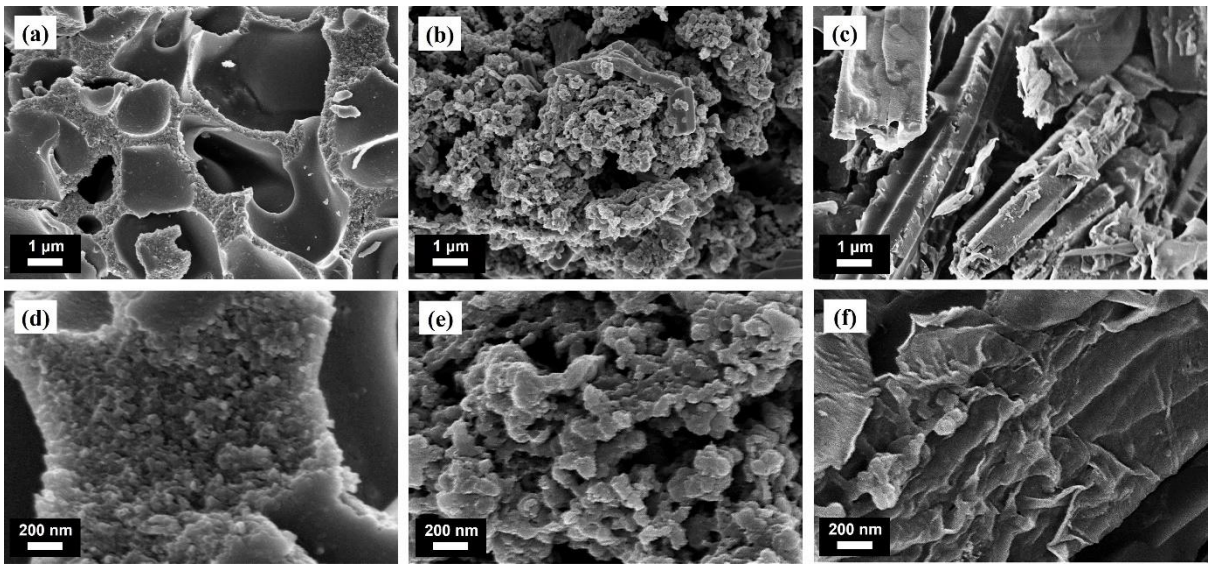

Figure 1: Low-magnification FESEM images of (a) Fe-N-C_HS, (b) Fe-N-C_B and (c) Fe-N-C_N. High-magnification FESEM images of (d) Fe-N-C_HS, (e) Fe-N-C_B and (f) Fe-N-C_N.

In the synthesis of Fe-N-C_HS, the zinc nitrate hexahydrate and 2-methylimidazole was used as the precursor to form ZIF-8, and in a typical synthesis for Fe-N-C-based catalyst this ZIF-8 ligands acts as the N and C source provider.[34,35] Fe ions were introduced by doping the Fe precursor into the ZIF-8 ligands. Subsequent high-temperature pyrolysis was vital for removing the Zn ions from the ligands, which eventually resulted in a highly porous carbon structure while simultaneously forming active Fe-N_4 sites.[29] The full removal of Zn ions from

Fe-ZIF-8 was confirmed by the absence of a Zn peak in the XRD spectra, as shown in Figure 2 (a). The dominant peaks at 26° and 44° were attributed to the (002) and (101) graphitic carbon planes, respectively, according to JCPDS (PDF#75-1621).[36,37] Moreover, the slight peaks at 30°, 36° and 63° indicated the presence of the Fe_2O_3 phase according to the ICDD No. 00-016-0653 database.[27] On the other hand, the formation of the bulky Fe-N-C structure of Fe-N-C_B was controlled by the amount of oxidizing agent and aniline used, and in this case, ammonium persulfate (APS) was employed as the oxidizing agent to grow the polyaniline. Due to the low amount of APS to aniline used (mass ratio of 2:1), the bulky structure of Fe-N-C was formed as polymerization occurred at a low oxidation degree.[18] As shown in the XRD spectra, there were two broad peaks at 26° and 44°, which corresponded to the (002) and (101) graphitic peaks, similar to Fe-N-C_HS. However, the (002) peak was broader, thus demonstrating a more amorphous carbon structure of the catalyst.[38] The addition of melamine in the precursor does not affect the structure of the Fe-PANI precursors but improves the degree of graphitization.[16] Meanwhile, the preparation of Fe-N-C_N was carried out by fully utilizing the large, flat surface of NaCl as the template. In the synthesis process, NaCl was coated with solvent-containing precursors to grow Fe-N-C on the template. The bianthryl monomer was added to produce a polymer chain hybridized with the FePc. During the annealing process, the bromine atoms are removed from the monomers, and covalent bonds are formed between each monomer, leading to the formation of a polymer chain.[31] This polymer chain hybridizes with FePc in the carbon sheet, resulting in the formation of a two-dimensional carbon structure. The subsequent annealing process promoted the polymerization process of the monomer, which resulted in the formation of thin layers of Fe-N-C. The XRD spectra for Fe-N-C_N revealed that there were no NaCl peaks, which confirmed the full removal of the NaCl template after the washing process. It was also observed that there were large numbers of sharp peaks in the XRD spectrum of Fe-N-C_N, which indicated that Fe-N-C_N possessed a crystalline carbon structure. Meanwhile, broad peaks at $2\theta = 26°$ and 44° were observed for Fe-N-C_HS and Fe-N-C_B, suggesting that they had a low degree of crystallinity of the graphitic carbon phase. The percentage of crystallinity of the Fe-N-C catalysts were calculated to be 11.6, 18.08 and 29.72% for Fe-N-C_HS, Fe-N-C_B and Fe-N-C_N, respectively.

The pore characteristics of the Fe-N-C catalysts were further investigated through the N_2 adsorption-desorption method. Prior to N_2 physisorption, the samples were degassed at 150 °C for 8 hours under high-vacuum conditions to remove all the contaminants from the surface. The N_2 adsorption-desorption isotherms were recorded at 77 K and presented in Figure 2 (b).

From the isotherm, it can be seen that there was a sharp increase in the adsorption slope at P/P_o < 0.2 for Fe-N-C_HS. This indicated the presence of micropores on the Fe-N-C_HS surface. In addition, the adsorption volume continuously increased as the relative pressure increased towards a P/P_o of 1.0, thereby revealing that Fe-N-C_HS displayed a type IV isotherm with hysteresis loop type 2 (according to IUPAC),[39] signifying a large mesopore structure on the Fe-N-C_HS surface. In contrast, Fe-N-C_B and Fe-N-C_N both displayed type II isotherms, in which there were low adsorption slopes at P/P_o < 0.9, thus reflecting low micropore and mesopore formation on the catalysts. A sudden increase in the absorption peak at high relative pressure (P/P_o > 0.95) for both Fe-N-C_B and Fe-N-C_N was noticeable, implying that there were macropores on the surface. Their hysteresis loops implies type 4 hysteresis, suggesting a narrow slit-like pores.[40,41] The interpretation of this isotherm linear plot was in good agreement with the interpretation of the surface morphology of the Fe-N-C catalyst from the FESEM and TEM images. The high number of mesopores in Fe-N-C_HS were attributed to the voids between the nanoparticles, while the absence of micro- and mesopores in both Fe-N-C_B and Fe-N-C_N resulted from the dense agglomeration of the bulk Fe-N-C, which obstructed the interspace voids.[28,42]

As shown in the BJH analysis presented in Figure 2 (c), Fe-N-C_HS displayed a high number of pores with diameters less than 2 nm, which indicated that this Fe-N-C_HS structure was dominated by micropores. The formation of these micropores resulted from the formation of Fe-N_x sites during high-temperature carbonization.[43,44] Meanwhile, from the BJH, Fe-N-C_B exhibited a wide range of pore width distributions, which indicated that Fe-N-C_B had a hierarchical porous structure with the presence of micro-, meso- and macropores.[45] The same BJH adsorption plot trend was observed for Fe-N-C_N, with a slight decrease in the volume of macropores. This was due to the 2D-like nature of Fe-N-C_N with a smooth surface compared to the agglomerated bulk structure of Fe-N-C_B. The percentage of the micropore area are Further investigation of the pore volume was conducted by applying the BJH method using N_2 adsorption at P/P_o = 0.978.[46] The BET surface area, t-plot micropore area and BJH pore volume are tabulated in Table 1. The surface area of the Fe-N-C catalyst calculated from the BET analysis shows a decreasing order of Fe-N-C_HS > Fe-N-C_B > Fe-N-C_N. The high surface area of Fe-N-C_HS was correlated with its hollow sphere structure with an abundance of micro- and mesopores, while Fe-N-C_N had the lowest BET surface area due to its thin sheet-like structure, in which there could be a stacking between layers as observed in Figure 1 (c, f), similar to graphene layers structure, thus reducing the exposed surface area.[47] Notably, Fe-N-

C_N demonstrates lowest percentage of micropores and is dominated by macropores. In contrast, Fe-N-C_HS had the highest surface area (492.7 m^2/g), with large percentage of micropores (51.14%) and lowest amount of macropores. The presence of micropores is beneficial for the ORR, with common consensus that the active sites of FeN_x are located.[48] Moreover, the presence of mesopores is important for facilitating the mass transport of the reactant to the active sites.[49,50] According to Lee et al., the mesopores are beneficial for wetting the physical surface area of the catalyst by the electrolyte, thus increasing the number of accessible active sites.[51] Mesopores improve the ability of the electrolyte to penetrate the catalyst surface, which increases the number of active sites available for the reaction.[48] Herein, Fe-N-C_B shows a good balance between micropores, mesopores and macropores based on Figure 2(c) and Table 1. It is expected that the high surface area with an abundance of both micro- and mesopores of Fe-N-Cs with the presence of active sites such as FeN_x and N-C bonds can exhibit good ORR activity, especially in acidic medium.

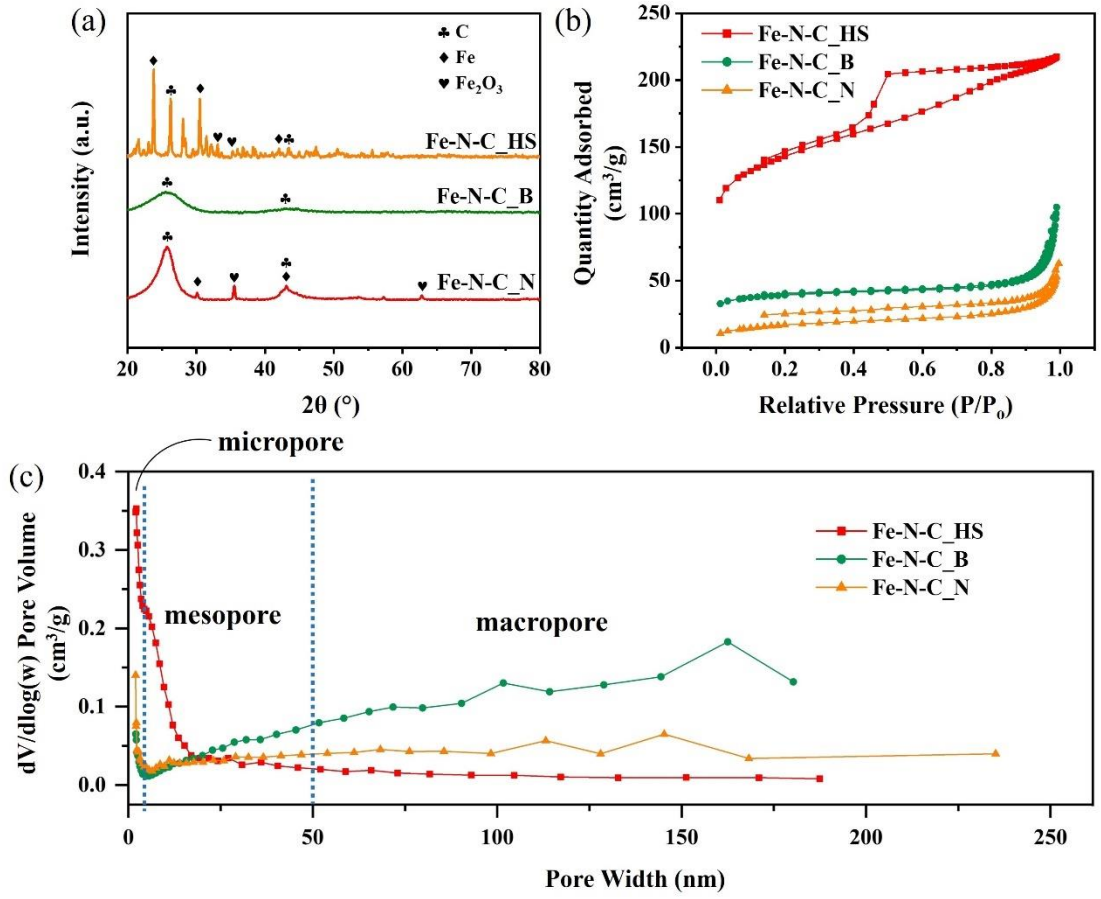

Figure 2: (a) XRD spectra, (b) N_2 adsorption-desorption isotherm and (c) BJH pore distribution of Fe-N-C_HS, Fe-N-C_B and Fe-N-C_N.

Table 1: Surface properties of Fe-N-C_HS, Fe-N-C_B and Fe-N-C_N

Sample	S_{BET} (m^2/g)[a]	S_{micro} (m^2/g)[b]	V_{total} (m^3/g)[c]	D_{avg} (nm)[d]	Percentage of micropore area (%)
Fe-N-C_HS	492.7	251.97	0.33	3.5	51.14
Fe-N-C_B	133.3	91.78	0.15	17.4	68.85
Fe-N-C_N	61.3	10.34	0.08	9.6	16.87

[a] Multipoint BET surface area calculated from N_2 adsorption-desorption

[b] Micropore area measured using the t-plot method

[c] Single-point desorption total pore volume of pores less than 911.245 Å width at P/P_o = 0.978

[d] BJH desorption average pore diameter

The surface chemistry of the catalysts was analysed using XPS. After the XPS measurements, the XPS spectra were corrected by using the C 1s peak at 284.8 eV as a reference before further analysis.[52] Figure 3 (a) shows the XPS survey spectra of Fe-N-C_HS, Fe-N-C_B and Fe-N-C_N, where there were obvious peaks at C 1s, N 1s, O 1s and Fe 2p, thus revealing the presence of Fe, N, C and O elements on the catalysts. The atomic percentages of these elements are tabulated in Table 2. As shown in the survey spectra, Fe-N-C_HS exhibited a low intensity of N 1s and Fe 2p peaks compared to the other two Fe-N-C samples. The low amount of N and Fe content in Fe-N-C_HS suggested the formation of Fe single atom with Fe-N bonding during the doping of Fe ions on ZIF-8[53] as well as the high-temperature heat treatment during the synthesis.[29] The formation of single-atom Fe-N bonding is believed to allow 100% utilization of Fe particles in the reaction and therefore enhancing the ORR activity.[54,55] A low N-peak intensity was observed due to the reduced nitrogen content caused by the decomposition and volatilization of nitrogen at high temperature.[56] Only stable N-bonds will remain. The N contents of all the Fe-N-C catalyst were in the range of 1.26–9.71 at.%. The variations in the N content were due to the thermal stabilities of nitrogen species. According to Xiao et al., graphitic-N are the most stable nitrogen bonding at higher temperatures, followed by pyridinic-N and pyrrolic-N.[24]

Further analysis to investigate the state of Fe and N were carried out. As shown in Figure 3 (b), the high-resolution spectra of Fe 2p of all the Fe-N-C catalyst displayed a Fe $2p_{1/2}$ peak at 711.0 eV and Fe $2p_{3/2}$ peak at 724.7 eV. The XPS spectra of Fe 2p was deconvoluted

into Fe^{2+}, Fe^{3+} and satellite, which indicated the formation of Fe_3O_4.[57] High-resolution spectra of N 1s were recorded and deconvoluted into four species in the range of 396–406 eV with peak centres at 398.5 eV, 399.4 eV, 400.4 eV and 401.3 , which were assigned to pyridinic-N, Fe-N_x, pyrrolic-N and graphitic-N, respectively.[58,59] The N 1s peak fittings are shown in Figure 3 (c). Generally, the ORR activity of a catalyst depends on the nitrogen functionality,[45] where the types of nitrogen bonding contribute to the ORR. Pyridinic-N provides active sites for the ORR by coordinating with atomic Fe to generate FeN_x coordination, while graphitic-N is beneficial because it improves the kinetic current, and pyrrolic-N is advantageous for reducing the O_2 to H_2O_2 via the $2e^-$ ORR pathway.[60-62] As indicated by the fitted peak of N 1s of Fe-N-C_HS, dominant graphitic-N was present (54.38 at.%), followed by pyrrolic-N (33.04 at.%) Fe-N_x (8.98 at.%) and pyridinic-N (3.60 at.%). The Fe-N-C_B has high number of graphitic-N, followed by pyridinic-N, Fe-N_x and pyrrolic-N, with the atomic percentage of 53.31, 22.46, 20.25, 3.98 at.%, respectively. Meanwhile, the Fe-N-C_N has 42.01, 28.69, 21.90 and 7.3 at.% of pyridinic-N, Fe-N_x, pyrrolic-N and graphitic-N, respectively. According to Luo et al., pyridinic-N and pyrrolic-N are located on the exposed edge planes, thus contributing to the ORR activity.[63] No oxidized nitrogen was detected for any of the Fe-N-C catalysts. According to Wen et al., the oxidized nitrogen is barely associated to the oxygen reduction performance.[42] The content of the respective nitrogen bonding of each Fe-N-C catalysts is presented in Figure 3 (d).

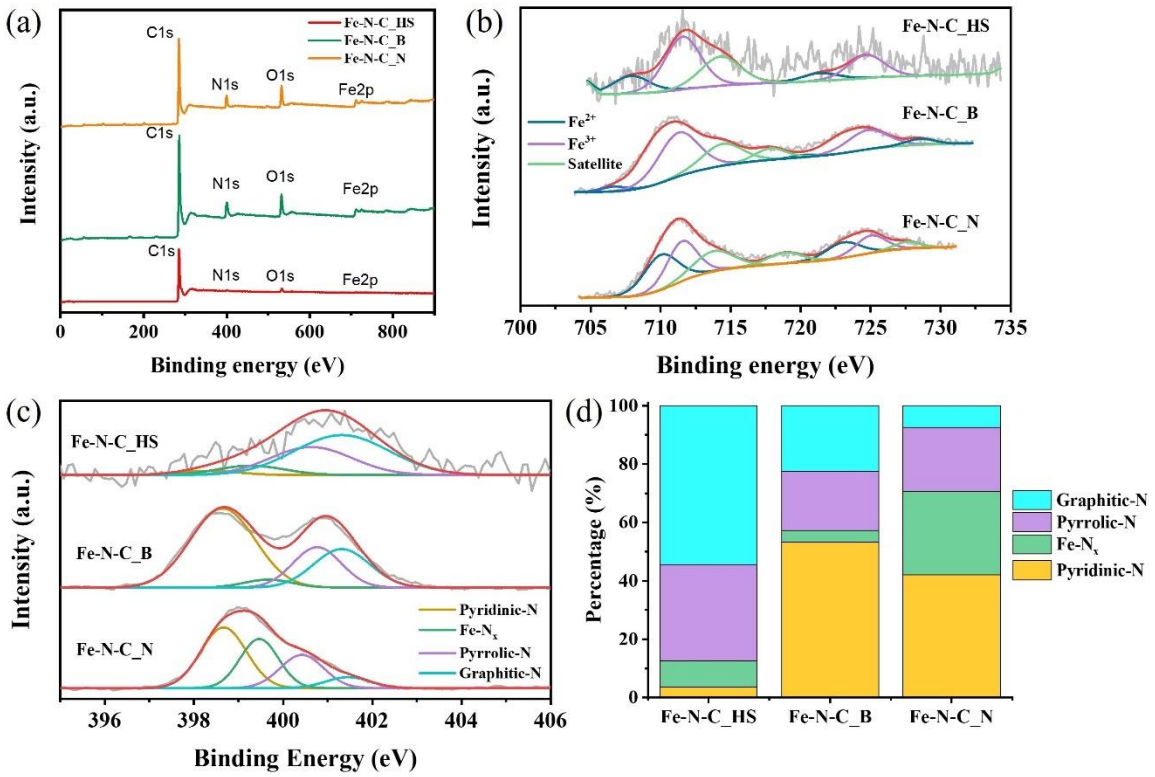

Figure 3: (a) XPS survey spectra, (b) high-resolution Fe 2p spectra, (c) high-resolution N 1s spectra, and (d) atomic percentage of nitrogen species of Fe-N-C_HS, Fe-N-C_B and Fe-N-C_N.

Table 2: Chemical composition determined through XPS analysis.

Sample	Elemental composition (at.%)				N 1s (at.%)			
	Fe	N	C	O	Pyridinic-N	Fe-N_x	Pyrrolic-N	Graphitic-N
Fe-N-C_HS	0.08	1.26	96.62	3.04	3.60	8.98	33.04	54.38
Fe-N-C_B	1.57	9.71	80.79	7.93	53.31	3.98	20.25	22.46
Fe-N-C_N	1.53	8.32	80.5	9.65	42.01	28.69	21.90	7.3

3.2 Analysis of the ORR

The electrochemical reactions of the Fe-N-C catalysts in alkaline medium were identified through CV in O_2 and N_2 environments, as shown in Figure 4 (a-c). In 0.1 M KOH, it was observed that there were prominent reduction peaks at 0.78, 0.74 and 0.76 V vs. RHE

for Fe-N-C_HS, Fe-N-C_B and Fe-N-C_N, respectively, which indicated that oxygen reduction occurred. The catalytic activity of these Fe-N-C catalysts were assessed through LSV, as shown in Figure 4 (d). A remarkable onset potential was demonstrated by Fe-N-C_HS, similar to Pt/C with E_{onset} of 0.95 V vs. RHE, while Fe-N-C_B and Fe-N-C_N possess the E_{onset} of 0.93 and 0.92 V vs. RHE, respectively. However, the limiting current density of Fe-N-C_HS was low. This indicated a low mass transfer rate of oxygen to the catalyst surface.[64] This can occur due to a number of factors, such as poor oxygen diffusion through the electrode or the low surface area of a catalyst.[65] Despite having the highest surface area, the decreased activity of Fe-N-C_HS was attributed to the nonuniform distribution of Fe-based nanoparticles, obstructing access to the active N-C sites.[66] On the other hand, Fe-N-C_B showed a superior current density of 3.26 mA cm^{-2} compared to the other Fe-N-C catalysts, 2.48 and 2.42 mA cm^{-2} for Fe-N-C_HS and Fe-N-C_N, respectively. A microkinetic study was further conducted to study the ORR mechanism, in which all the Fe-N-C exhibited a Tafel slope lower than 60 mV dec^{-1}. In general, a smaller Tafel slope indicates that the reaction is kinetically more favourable and that the electrocatalyst has a higher activity for the ORR.[67] Generally, the ORR can occur through either a four-electron pathway or a two-electron pathway or a combination of both. However, the two-electron pathway is less favourable, as it is kinetically slower and produces intermediate products (OOH^-) that can harm the electrode. Further calculations of the electron transfer number were conducted through the RRDE method to investigate the reaction pathway. As shown in Figure 4 (f), the electron transfer numbers were all above 3.6 and in the order of Fe-N-C_B > Fe-N-C_HS > Fe-N-C_N. This indicated that these Fe-N-C catalysts exhibit a 4-electron transfer pathway in alkaline medium. Through RRDE, the OOH^- content was also calculated, and all the Fe-N-C catalysts produced OOH^- at percentages less than 20%. From this ORR electrochemical investigation, it was observed that Fe-N-C_B showed superior ORR activity in alkaline media. This was correlated to its highest N content, which not only enhance the electronic conductivity of the catalyst but also contributed to the formation of a highly active electrocatalytic surface.[68] The morphology of Fe-N-C catalysts can also influence the electronic structure and coordination environment of active sites, which can affect their ORR activity. Fe-N-C_B, with a hierarchical porous structure has a good distribution of micro-, meso- and macropores. This leads to the high formation of pyridinic-N which are usually located at the micro- and mesopores. These pyridinic-N are beneficial for the catalytic activity of the ORR in alkaline media. In contrast, despite having a higher surface area, Fe-N-C_HS has a very low amount of pyridinic-N which are the main active site for the ORR in alkaline media. In addition, the highly mesoporous structure found in Fe-N-C_B facilitates mass

transport of reactants and products between the catalyst and the electrolyte, while the macropores provide channels for efficient gas diffusion.[69] This porous structure allows for better access of reactants and products to the active sites of the catalyst, thereby improving the catalytic activity and efficiency.

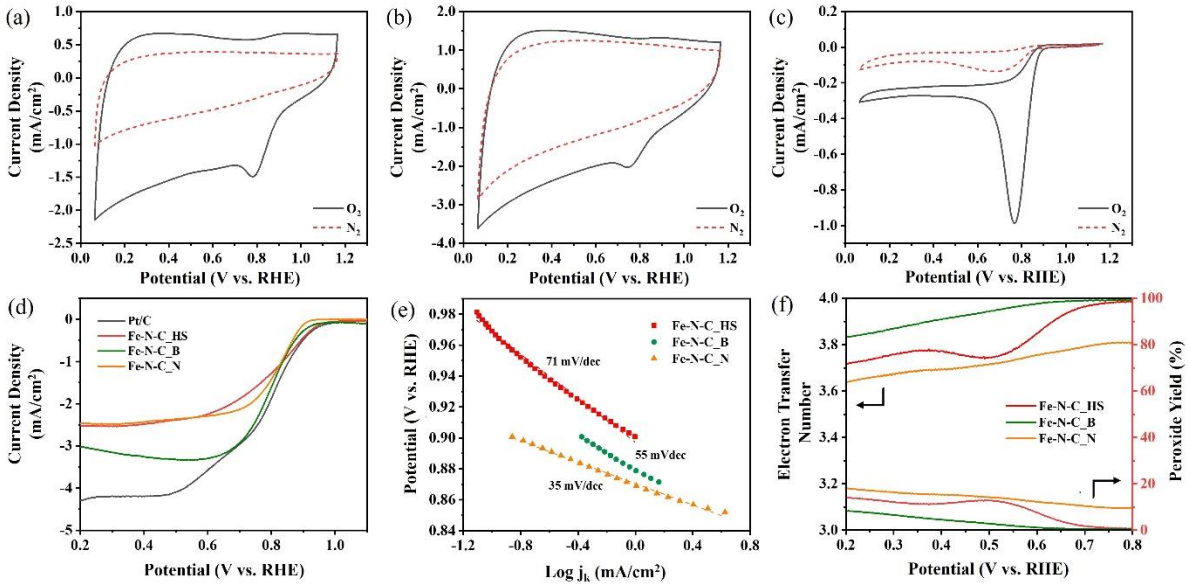

Figure 4: Cyclic voltammetry (CV) of (a) Fe-N-C_HS, (b) Fe-N-C_B, and (c) Fe-N-C_N, (d) Linear sweep voltammetry (LSV), (e) Tafel slope, and (f) electron transfer number and hydrogen peroxide production of Fe-N-C_HS, Fe-N-C_B, and Fe-N-C_N in 0.1 M KOH.

The ORR behaviour of the Fe-N-C catalysts was also investigated in an acidic media. As shown in the recorded CV (Figure 5 (a-c)), Fe-N-C_HS and Fe-N-C_B exhibited ORR activity, with obvious ORR peaks under O_2-saturated acidic electrolyte. Meanwhile, Fe-N-C_N was found to be catalytically inactive due to the absence of an ORR peak. As shown in the LSV in Figure 5 (d), Fe-N-C_HS possessed the highest onset potential (E_{onset} = of 0.83 V vs. RHE), followed by Fe-N-C_B (E_{onset} = 0.80 V vs. RHE) and Fe-N-C_N (E_{onset} = 0.55 V vs. RHE). From Figure 5 (e), Fe-N-C_HS exhibited the lowest Tafel slope of 141 mV dec^{-1}, which indicated that a one-electron transfer was the rate determining step. The same observation was seen for Fe-N-C_B, with a Tafel slope of 145 mV dec^{-1}. Nevertheless, the Tafel slope exhibited by Fe-N-C_N was high and at a very high overpotential, thus indicating its poor ORR activity. This is because, Fe-N-C_N has a sheet-like structure with low micropores where FeN_x are located. Furthermore, it can be observed from the TEM image in Figure 7 that the Fe particles are aggregating on the surface of Fe-N-C_N and obstruct the active sites. The electron transfer number calculated through the RRDE method revealed that both Fe-N-C_HS and Fe-N-C_B

yielded outstanding four-electron transfer numbers of n = 3.96 and 3.91, respectively, while Fe-N-C_N exhibited a decrease in the electron transfer number. This correlates with the amount of H_2O_2 produced.[70] In fact, the higher the amount of hydrogen peroxide produced, the slower the ORR kinetics because the dissociative adsorption of O_2 species in the inner sphere is impeded by the presence of oxygen-based species.[71] From the electrochemical measurements, it can be deduced that Fe-N-C_HS shows the highest ORR activity in acidic medium, followed by Fe-N-C_B. Meanwhile, Fe-N-C_N are not favourable for ORR in acidic medium. These results indicated that there was a strong relationship between the surface area of a catalyst and its onset potential, by which larger surface areas provide more active sites for the reactions to occur. The high BET surface area and pore volume of Fe-N-C_HS contributed to its exceptional catalytic activity. A high pore volume enhances the transport of reactant species to the active sites, which are believed to be located in the micropores of the catalyst.[72] Notably, the high amount of Fe-N_x sites presented in Fe-N-C_HS is advantageous for the ORR to occur in acidic medium.

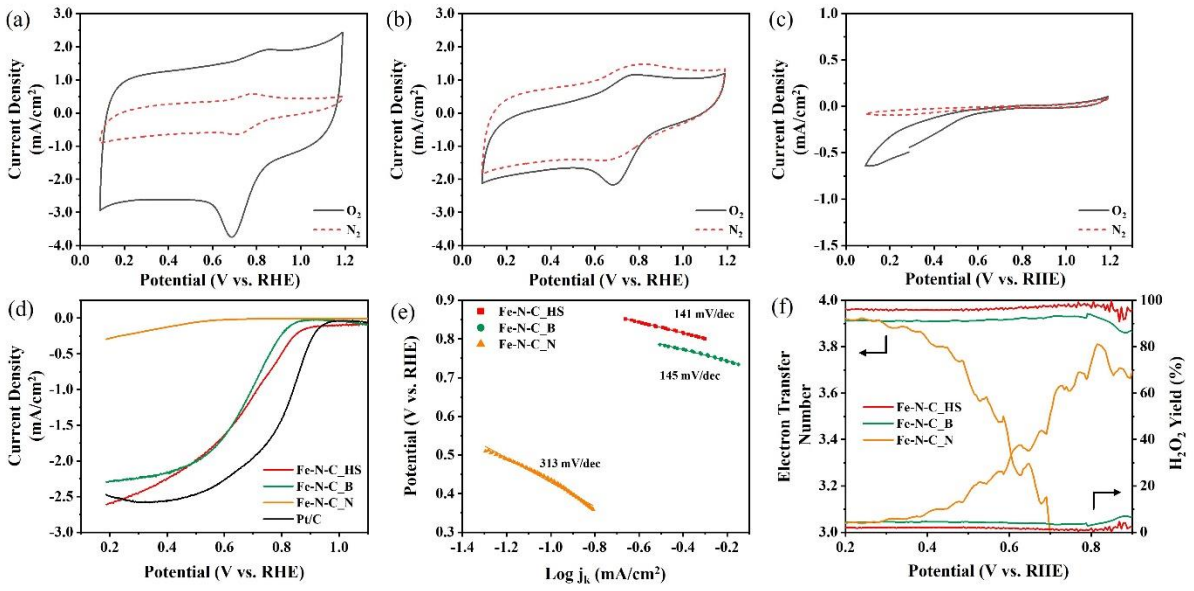

Figure 5: Cyclic voltammetry (CV) of (a) Fe-N-C_HS, (b) Fe-N-C_B, and (c) Fe-N-C_N. (d) Linear sweep voltammetry (LSV), (e) Tafel slope, and (f) electron transfer number and hydrogen peroxide production of Fe-N-C_HS, Fe-N-C_B, and Fe-N-C_N in 0.1 M $HClO_4$.

The catalyst durability was further studied using an ADT with the load cycling protocol reported in other studies.[32,73] As shown in Figure 6 (a), there was no attenuation of the half-wave potential of Fe-N-C_HS after 5,000 cycles of ADT load cycles in 0.1 M KOH. However, it was observed that the current density started to drop after the ADT cycles. This could be due

to the deterioration of the catalyst and electrode.[74] On the other hand, Fe-N-C_B showed an improvement in the current after the ADT cycles with no attenuation of the onset and half-wave potential (Figure 6 (b)), while Fe-N-C_N showed a slight increase in the onset potential after the ADT (Figure 6 (c)). The durability of the catalysts was also tested in an acidic 0.1 M $HClO_4$ environment. The same ADT protocol was employed, with a potential window between 0.2 and 0.75 V vs. Ag/AgCl, which corresponded to the 0.5 to 1.0 V vs. RHE that was used for the ADT in 0.1 M $HClO_4$ electrolyte. Figure 6 (d, e) shows that the half-wave potential of Fe-N-C_HS and Fe-N-C_B improved after 5,000 ADT cycles, indicating the activation of active sites during the cycles. This can be attributed to catalyst activation, which may be a result of the improved dispersion of Fe-N-C particles on the electrode surface, leading to a higher density of accessible active sites and an enhanced ORR reaction. On the other hand, Fe-N-C_N exhibited a low durability, as shown in Figure 6 (f). The major contributing factors that degrade the catalysts and cause performance decay are metal leaching, carbon corrosion, the presence of H_2O_2 and protonation of active sites.[75]

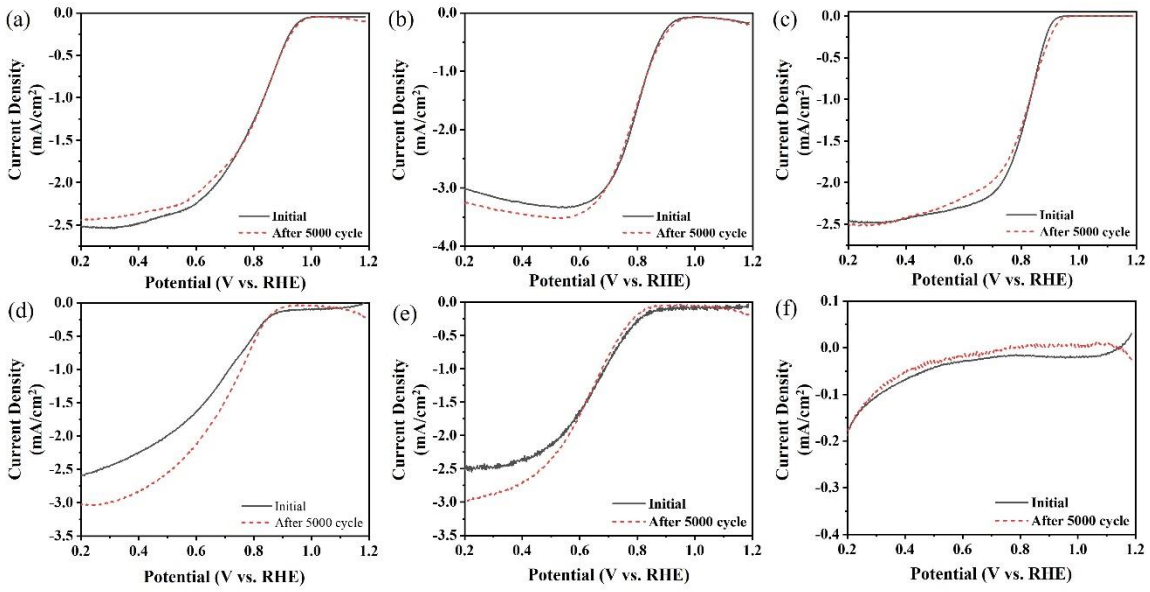

Figure 6: Linear sweep voltammetry (LSV) of (a) Fe-N-C_HS, (b) Fe-N-C_B and (c) Fe-N-C_N before and after the ADT in 0.1 M KOH. Linear sweep voltammetry (LSV) of (d) Fe-N-C_HS, (e) Fe-N-C_B and (f) Fe-N-C_N before and after the ADT in 0.1 M $HClO_4$.

To further investigate the change in the morphology of the Fe-N-C catalysts, we observed the structure of the catalyst before and after the ADT using TEM imaging. As shown

in Figure 7, the TEM image revealed that the particles were less agglomerated and started to loosen, generating interparticle gaps after 5,000 ADT cycles under both alkaline and acidic conditions. This was caused by the high resistance of the catalyst towards electrochemical degradation.[33] The increase in the surface area provides an increase in the mass transport of the reactant to the active sites of the catalyst.[76] On the other hand, the TEM image of Fe-N-C_N showed an increase in the particle diameter post-ADT, which led to a decrease in the surface area, as shown by the TEM image in Figure 7 (c).

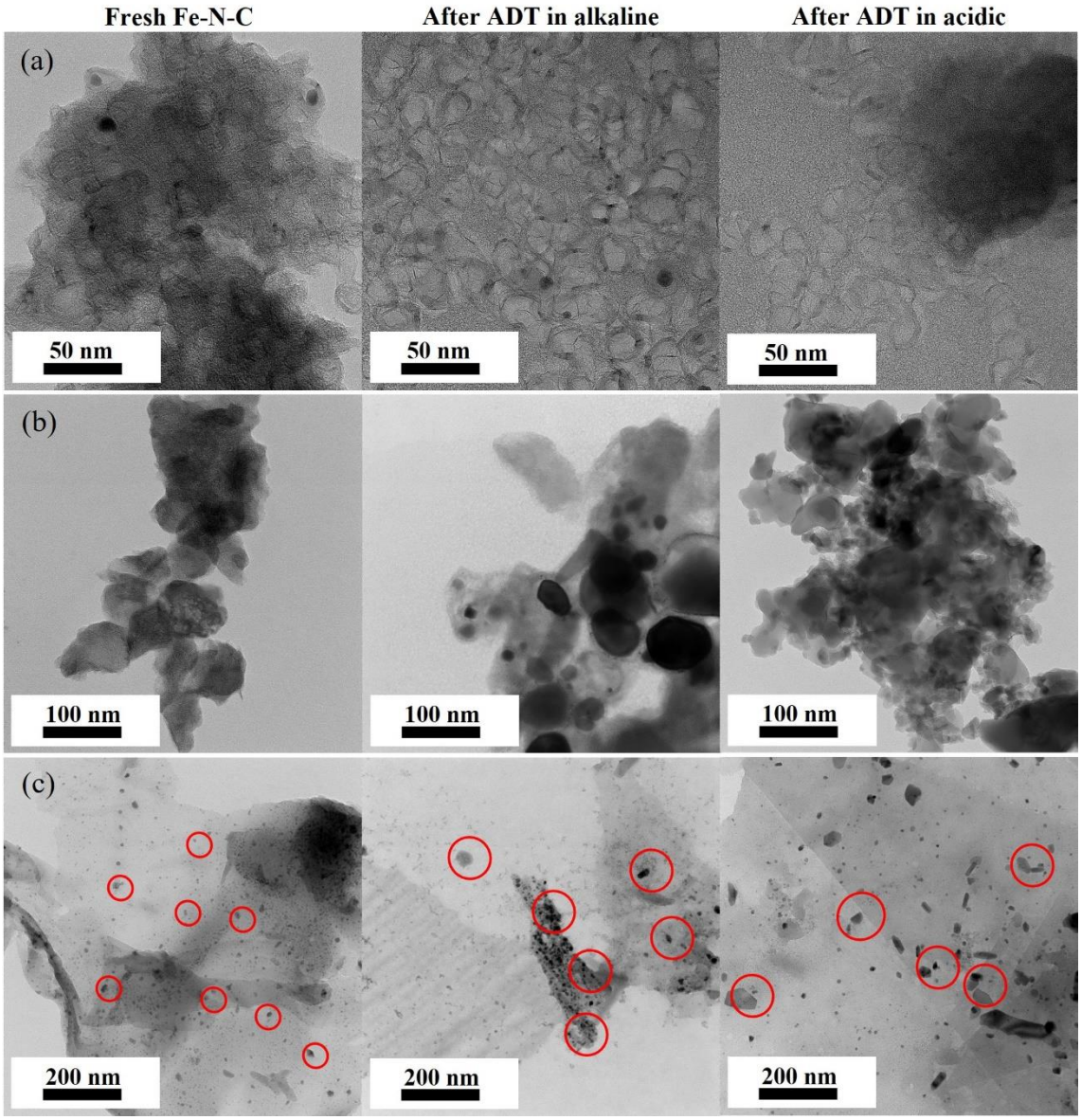

Figure 7: TEM image of fresh sample and after 5,000 ADT cycles in alkaline and acidic conditions of (a) Fe-N-C_HS, (b) Fe-N-C_B and (c) Fe-N-C_N. Areas circled red in (c) indicates an overall increase in the particle diameter,

The stability of the catalysts in both alkaline and acidic environments was further investigated through a chronoamperometry test. The continuous chronoamperometric measurements were performed for 10,000 s at 0.6 V vs. RHE in O_2-saturated electrolyte to obtain the current-time response. As shown in Figure 8, Fe-N-C_HS was the most stable catalyst, retaining more than 93% and 80% of the current over 10,000 s in alkaline and acidic electrolytes, respectively. Meanwhile, the commercial Pt/C catalyst only maintained 80% and 61% of current in both alkaline and acidic electrolytes, respectively. The poor stability that caused an enormous current loss during the chronoamperometry test of Pt/C was mainly due to carbon corrosion and Pt dissolution, which especially occurs under an acidic environment.[77] Meanwhile, for Fe-N-C_B, the presence of graphitized carbon layers was beneficial for maintaining the current stability in both alkaline and acidic environments by preventing Fe aggregation and dissolution.[78] On the other hand, Fe-N-C_N showed the worst current stability and only retained a current of less than 40% after 10,000 s in an acidic environment. This was correlated with the high amount of H_2O_2 produced, which led to carbon corrosion, especially at low potential.[79,80]

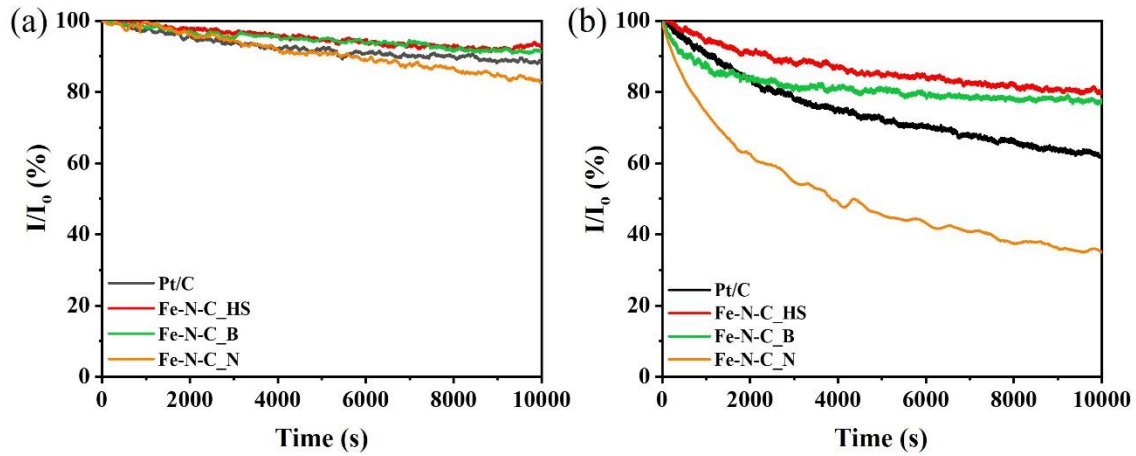

Figure 8: Current-time curve from the chronoamperometry test in a) 0.1 M KOH and b) 0.1 M $HClO_4$.

4.0 Conclusion

From the above series of characterizations, it was confirmed that the Fe-N-C catalyst morphology does affect its electrocatalytic activity towards the ORR, with a significant effect on its activity and stability during the ORR. A catalyst with a higher surface area and more accessible active sites tends to have a higher ORR activity than a catalyst with a lower surface

area. Additionally, the stability and durability of the catalysts were also influenced by the morphology. Therefore, understanding the effect of morphology on Fe-N-C catalysts is important for the development of high-performance ORR catalysts for fuel cell applications. A balance of meso- and micropores, as well as a high pore volume, improve the mass transport of reactants to the centres of the active sites. Thus, the morphology of the catalyst is a key factor in achieving high ORR activity through a high specific surface area.

Acknowledgement

This project was funded by the Ministry of Higher Education (MOHE) Malaysia through the Fundamental Research Grant Scheme (project code: FRGS/1/2019/STG01/UKM/02/2) and H2Green (Ningbo) New Energy Technology Co., Ltd., China (RA-2022-004). The authors would like to acknowledge the Malaysian Nuclear Agency and Centre for Research and Instrumentation Universiti Kebangsaan Malaysia (iCRIM) for providing the analysis facilities for this project.

References

1. Xu J, Liang G, Chen D, Li Z, Zhang H, Chen J, Xie F, Jin Y, Wang N, and Meng H, Iron and nitrogen doped carbon derived from ferrocene and ZIF-8 as proton exchange membrane fuel cell cathode catalyst. *Applied Surface Science* 2022;573:151607.
2. Ahmad Junaidi NH, Wong WY, Loh KS, Rahman S, and Daud WRW, A comprehensive review of MXenes as catalyst supports for the oxygen reduction reaction in fuel cells. *International Journal of Energy Research* 2021;45:15760-15782.
3. Huang B, Zhang X, Cai J, Liu W, and Lin S, A novel MnO_2/rGO composite prepared by electrodeposition as a non-noble metal electrocatalyst for ORR. *Journal of Applied Electrochemistry* 2019;49:767-777.
4. Lian J, Zhao J-Y, and Wang X-M, Recent Progress in Carbon-based Materials of Non-Noble Metal Catalysts for ORR in Acidic Environment. *Acta Metallurgica Sinica (English Letters)* 2021;34:885-899.
5. Zhang S, Chen M, Zhao X, Cai J, Yan W, Yen JC, Chen S, Yu Y, and Zhang J, Advanced Noncarbon Materials as Catalyst Supports and Non-noble Electrocatalysts for Fuel Cells and Metal–Air Batteries. *Electrochemical Energy Reviews* 2021;4:336-381.
6. Kiani M, Tian XQ, and Zhang W, Non-precious metal electrocatalysts design for oxygen reduction reaction in polymer electrolyte membrane fuel cells: Recent advances, challenges and future perspectives. *Coordination Chemistry Reviews* 2021;441:213954.
7. Sapkota P and Aguey-Zinsou K-F, Iron and tin phosphide as polymer electrolyte membrane fuel cell cathode catalysts. *International Journal of Hydrogen Energy* 2023;48:257-267.
8. Dong F, Wu M, Chen Z, Liu X, Zhang G, Qiao J, and Sun S, Atomically Dispersed Transition Metal-Nitrogen-Carbon Bifunctional Oxygen Electrocatalysts for Zinc-Air Batteries: Recent Advances and Future Perspectives. *Nano-Micro Letters* 2021;14:36.
9. Lee J, Seol C, Kim J, Jang S, and Kim SM, Optimizing Catalyst Loading Ratio between the Anode and Cathode for Ultralow Catalyst Usage in Polymer Electrolyte Membrane Fuel Cell. *Energy Technology* 2021;9:2100113.
10. Zhang M, Yang B, Yang T, Yang Y, and Xiang Z, A ferric citrate derived Fe-N-C electrocatalyst with stepwise pyrolysis for highly efficient oxygen reduction reaction. *Chinese Chemical Letters* 2022;33:362-367.
11. Wang Y, Chen L, Lai Y, Wang Y, Wang K, and Song S, MOF-Derived Porous Fe-N-C Materials for Efficiently Electrocatalyzing the Oxygen Reduction Reaction. *Energy & Fuels* 2022;36:5415-5423.
12. Huang J-W, Chen Y-B, Yang J-M, Zhu H-B, and Yang H, Boosting the oxygen reduction performance of MOF-5-derived Fe-N-C electrocatalysts via a dual strategy of cation-exchange and guest-encapsulation. *Electrochimica Acta* 2021;366:137408.
13. Xie X, Shang L, Xiong X, Shi R, and Zhang T, Fe Single-Atom Catalysts on MOF-5 Derived Carbon for Efficient Oxygen Reduction Reaction in Proton Exchange Membrane Fuel Cells. *Advanced Energy Materials* 2022;12:2102688.
14. Lin Y-J, Tsai J-E, Huang C-C, Chen Y-S, and Li Y-Y, Highly Porous Iron-Doped Nitrogen–Carbon Framework on Reduced Graphene Oxide as an Excellent Oxygen Reduction Catalyst for Proton-Exchange Membrane Fuel Cells. *ACS Applied Energy Materials* 2022;5:1822-1832.

15. Xu X, Zhang X, Xia Z, Sun R, Li H, Wang J, Yu S, Wang S, and Sun G, Solid phase microwave-assisted fabrication of Fe-doped ZIF-8 for single-atom Fe-N-C electrocatalysts on oxygen reduction. *Journal of Energy Chemistry* 2021;54:579-586.
16. Mahmood A, Xie N, Zhao B, Zhong L, Zhang Y, and Niu L, Optimizing Surface N-Doping of Fe-N-C Catalysts Derived from Fe/Melamine-Decorated Polyaniline for Oxygen Reduction Electrocatalysis. *Advanced Materials Interfaces* 2021;8:2100197.
17. Gupta S, Zhao S, Ogoke O, Lin Y, Xu H, and Wu G, Engineering Favorable Morphology and Structure of Fe-N-C Oxygen-Reduction Catalysts through Tuning of Nitrogen/Carbon Precursors. *ChemSusChem* 2017;10:774-785.
18. He Q, Chen X, Jia F, Ding W, Zhou Y, Wang J, Song X, Jiang J, Liao Q, Li J, and Wei Z, The Role of Polyaniline Molecular Structure in Producing High-Performance Fe-N-C Catalysts for Oxygen Reduction Reaction. *ChemistrySelect* 2019;4:8135-8141.
19. Sgarbi R, Kumar K, Jaouen F, Zitolo A, Ticianelli EA, and Maillard F, Oxygen reduction reaction mechanism and kinetics on M-N_xC_y and M@N-C active sites present in model M-N-C catalysts under alkaline and acidic conditions. *Journal of Solid State Electrochemistry* 2021;25:45-56.
20. Huang X, Wu X, Niu Y, Dai C, Xu M, and Hu W, Effect of nanoparticle composition on oxygen reduction reaction activity of Fe/N–C catalysts: a comparative study. *Catalysis Science & Technology* 2019;9:711-717.
21. Liu S, Meyer Q, Li Y, Zhao T, Su Z, Ching K, and Zhao C, Fe–N–C/Fe nanoparticle composite catalysts for the oxygen reduction reaction in proton exchange membrane fuel cells. *Chemical Communications* 2022;58:2323-2326.
22. Yang S, Liu X, Niu F, Wang L, Su K, Liu W, Dong H, Yue H, and Yin Y, 2D Single-Atom Fe–N–C Catalyst Derived from a Layered Complex as an Oxygen Reduction Catalyst for PEMFCs. *ACS Applied Energy Materials* 2022;5:8791-8799.
23. Liu F, Yan N, Zhu G, Liu Z, Ma S, Xiang G, Wang S, Liu X, and Wang W, Fe–N–C single-atom catalysts with an axial structure prepared by a new design and synthesis method for ORR. *New Journal of Chemistry* 2021;45:13004-13014.
24. Xiao M, Zhu J, Ma L, Jin Z, Ge J, Deng X, Hou Y, He Q, Li J, Jia Q, Mukerjee S, Yang R, Jiang Z, Su D, Liu C, and Xing W, Microporous Framework Induced Synthesis of Single-Atom Dispersed Fe-N-C Acidic ORR Catalyst and Its in Situ Reduced Fe-N_4 Active Site Identification Revealed by X-ray Absorption Spectroscopy. *ACS Catalysis* 2018;8:2824-2832.
25. Jin X, Wang X, Liu Y, Kim M, Cao M, Xie H, Liu S, Wang X, Huang W, Nanjundan AK, Yuliarto B, Li X, and Yamauchi Y, Nitrogen and Sulfur Co-Doped Hierarchically Porous Carbon Nanotubes for Fast Potassium Ion Storage. *Small* 2022;18:2203545.
26. Kim M, Xu X, Xin R, Earnshaw J, Ashok A, Kim J, Park T, Nanjundan AK, El-Said WA, Yi JW, Na J, and Yamauchi Y, KOH-Activated Hollow ZIF-8 Derived Porous Carbon: Nanoarchitectured Control for Upgraded Capacitive Deionization and Supercapacitor. *ACS Applied Materials & Interfaces* 2021;13:52034-52043.
27. Sudarsono W, Wong WY, Loh KS, Majlan EH, Syarif N, Kok K-Y, Yunus RM, Lim KL, and Hamada I, Sengon wood-derived RGO supported Fe-based electrocatalyst with stabilized graphitic N-bond for oxygen reduction reaction in acidic medium. *International Journal of Hydrogen Energy* 2020;45:23237-23253.
28. Sudarsono W, Wong WY, Loh KS, Majlan EH, Syarif N, Kok K-Y, Yunus RM, and Lim KL, Noble-free oxygen reduction reaction catalyst supported on Sengon wood

(Paraserianthes falcataria L.) derived reduced graphene oxide for fuel cell application. *International Journal of Energy Research* 2020;44:1761-1774.
29. Zhang H, Hwang S, Wang M, Feng Z, Karakalos S, Luo L, Qiao Z, Xie X, Wang C, Su D, Shao Y, and Wu G, Single Atomic Iron Catalysts for Oxygen Reduction in Acidic Media: Particle Size Control and Thermal Activation. *Journal of the American Chemical Society* 2017;139:14143-14149.
30. Peng H, Mo Z, Liao S, Liang H, Yang L, Luo F, Song H, Zhong Y, and Zhang B, High Performance Fe- and N- Doped Carbon Catalyst with Graphene Structure for Oxygen Reduction. *Scientific Reports* 2013;3:1765.
31. Chung DY, Kim MJ, Kang N, Yoo JM, Shin H, Kim O-H, and Sung Y-E, Low-Temperature and Gram-Scale Synthesis of Two-Dimensional Fe–N–C Carbon Sheets for Robust Electrochemical Oxygen Reduction Reaction. *Chemistry of Materials* 2017;29:2890-2898.
32. Sinniah JD, Wong WY, Loh KS, Yunus RM, and Timmiati SN, Perspectives on carbon-alternative materials as Pt catalyst supports for a durable oxygen reduction reaction in proton exchange membrane fuel cells. *Journal of Power Sources* 2022;534:231422.
33. Wan X, Liu X, and Shui J, Stability of PGM-free fuel cell catalysts: Degradation mechanisms and mitigation strategies. *Progress in Natural Science: Materials International* 2020;30:721-731.
34. Zhe-qin C, Xiao-cong Z, Yong-min X, Jia-ming L, Zhi-feng X, and Rui-xiang W, A high-performance nitrogen-rich ZIF-8-derived Fe-NC electrocatalyst for the oxygen reduction reaction. *Journal of Alloys and Compounds* 2021;884:160980.
35. Tran T-N, Shin C-H, Lee B-J, Samdani JS, Park J-D, Kang T-H, and Yu J-S, Fe–N-functionalized carbon electrocatalyst derived from a zeolitic imidazolate framework for oxygen reduction: Fe and NH_3 treatment effects. *Catalysis Science & Technology* 2018;8:5368-5381.
36. Akram R, Ud Din MA, Dar SU, Arshad A, Liu W, Wu Z, and Wu D, From a ureidopyrimidinone containing organic precursor to excavated iron-nitrogen codoped hierarchical mesoporous carbon (Ex-FeN-MC) as an efficient bifunctional electrocatalyst. *Nanoscale* 2018;10:5658-5666.
37. Yin X, Chung H, Martinez U, Lin L, Artyushkova K, and Zelenay P, PGM-Free ORR Catalysts Designed by Templating PANI-Type Polymers Containing Functional Groups with High Affinity to Iron. *Journal of The Electrochemical Society* 2019;166:F3240-F3245.
38. Gupta S, Zhao S, Ogoke O, Lin Y, Xu H, and Wu G, Engineering Favorable Morphology and Structure of Fe-N-C Oxygen-reduction Catalysts via Tuning Nitrogen/Carbon Precursors. *ChemSusChem* 2016;10:
39. Sotomayor F, Cychosz K, and Thommes M, Characterization of Micro/Mesoporous Materials by Physisorption: Concepts and Case Studies. 2018;
40. Yurdakal S, Garlisi C, Özcan L, and Bellardita M, *(Photo)catalyst Characterization Techniques*. 2019. p. 87-152.
41. Monteverde Videla AHA, Osmieri L, Armandi M, and Specchia S, Varying the morphology of Fe-N-C electrocatalysts by templating Iron Phthalocyanine precursor with different porous SiO_2 to promote the Oxygen Reduction Reaction. *Electrochimica Acta* 2015;177:43-50.
42. Wen Y, Ma C, Wei Z, Zhu X, and Li Z, FeNC/MXene hybrid nanosheet as an efficient electrocatalyst for oxygen reduction reaction. *RSC Advances* 2019;9:13424-13430.

43. Mehmood A, Ali B, Gong M, Gyu Kim M, Kim J-Y, Bae J-H, Kucernak A, Kang Y-M, and Nam K-W, Development of a highly active FeNC catalyst with the preferential formation of atomic iron sites for oxygen reduction in alkaline and acidic electrolytes. *Journal of Colloid and Interface Science* 2021;596:148-157.
44. Yanhua LEI, Tan N, Zhu Y, Da H, Zhang Y, Sun S, and Gao G, Synthesis of Porous N-Rich Carbon/MXene from MXene@Polypyrrole Hybrid Nanosheets as Oxygen Reduction Reaction Electrocatalysts. *Journal of the Electrochemical Society* 2020;167:
45. Sauid SM, Kamarudin SK, Karim NA, and Shyuan LK, Superior stability and methanol tolerance of a metal-free nitrogen-doped hierarchical porous carbon electrocatalyst derived from textile waste. *Journal of Materials Research and Technology* 2021;11:1834-1846.
46. Zulkefli NN, Noor Azam AM, Masdar MS, and Isahak WN, Adsorption-Desorption Behavior of Hydrogen Sulfide Capture on a Modified Activated Carbon Surface. *Materials* 2023;16:
47. Yang Z, Yan X, Tang Z, Peng W, Zhang J, Tong Y, Li J, and Zhang J, Facile synthesis of hemin-based Fe-N-C catalyst by MgAl-LDH confinement effect for oxygen reduction reaction. *Applied Surface Science* 2022;573:151505.
48. Du L, Zhang G, Liu X, Hassanpour A, Dubois M, Tavares AC, and Sun S, Biomass-derived nonprecious metal catalysts for oxygen reduction reaction: The demand-oriented engineering of active sites and structures. *Carbon Energy* 2020;2:561-581.
49. Peng L, Yang J, Yang Y, Qian F, Wang Q, Sun-Waterhouse D, Shang L, Zhang T, and Waterhouse GIN, Mesopore-Rich Fe–N–C Catalyst with FeN_4–O–NC Single-Atom Sites Delivers Remarkable Oxygen Reduction Reaction Performance in Alkaline Media. *Advanced Materials* 2022;34:2202544.
50. Daniel G, Mazzucato M, Brandiele R, De Lazzari L, Badocco D, Pastore P, Kosmala T, Granozzi G, and Durante C, Sulfur Doping versus Hierarchical Pore Structure: The Dominating Effect on the Fe–N–C Site Density, Activity, and Selectivity in Oxygen Reduction Reaction Electrocatalysis. *ACS Applied Materials & Interfaces* 2021;13:42693-42705.
51. Lee SH, Kim J, Chung DY, Yoo JM, Lee HS, Kim MJ, Mun BS, Kwon SG, Sung Y-E, and Hyeon T, Design Principle of Fe–N–C Electrocatalysts: How to Optimize Multimodal Porous Structures? *Journal of the American Chemical Society* 2019;141:2035-2045.
52. Fang D, He F, Xie J, and Xue L, Calibration of Binding Energy Positions with C1s for XPS Results. *Journal of Wuhan University of Technology-Mater. Sci. Ed.* 2020;35:711-718.
53. Ding S, Barr JA, Shi Q, Zeng Y, Tieu P, Lyu Z, Fang L, Li T, Pan X, Beckman SP, Du D, Lin H, Li J-C, Wu G, and Lin Y, Engineering Atomic Single Metal–FeN_4Cl Sites with Enhanced Oxygen-Reduction Activity for High-Performance Proton Exchange Membrane Fuel Cells. *ACS Nano* 2022;16:15165-15174.
54. Noh WY, Kim EM, Kim KY, Kim JH, Jeong HY, Sharma P, Lee G, Jang J-W, Joo SH, and Lee JS, Immobilizing single atom catalytic sites onto highly reduced carbon hosts: Fe–N_4/CNT as a durable oxygen reduction catalyst for Na–air batteries. *Journal of Materials Chemistry A* 2020;8:18891-18902.
55. Huang J, Zhang Q, Ding J, and Zhai Y, Fe–N–C single atom catalysts for the electrochemical conversion of carbon, nitrogen and oxygen elements. *Materials Reports: Energy* 2022;2:100141.

56. Liu B, Huang B, Lin C, Ye J, and Ouyang L, Porous carbon supported Fe-N-C composite as an efficient electrocatalyst for oxygen reduction reaction in alkaline and acidic media. *Applied Surface Science* 2017;411:487-493.
57. Tan L, Xia Y, Wang S, Fang X, Yu Y, Jiang F, and Chen H, Hierarchical porous−enhanced peroxymonosulfate activation via 3D ordered macro−microporous Fe−NC: Role of high−valent iron−oxo species and electron−transfer mechanism. *Journal of Cleaner Production* 2023;383:135500.
58. Thomas M, Illathvalappil R, Kurungot S, Nair BN, Mohamed AP, Anilkumar GM, Yamaguchi T, and Hareesh US, Morphological Ensembles of N-Doped Porous Carbon Derived from ZIF-8/Fe-Graphene Nanocomposites: Processing and Electrocatalytic Studies. *ChemistrySelect* 2018;3:8688-8697.
59. Zhao Y-M, Zhang P-C, Xu C, Zhou X-Y, Liao L-M, Wei P-J, Liu E, Chen H, He Q, and Liu J-G, Design and Preparation of Fe–N_5 Catalytic Sites in Single-Atom Catalysts for Enhancing the Oxygen Reduction Reaction in Fuel Cells. *ACS Applied Materials & Interfaces* 2020;12:17334-17342.
60. Li Y, Liu T, Yang W, Zhu Z, Zhai Y, Gu W, and Zhu C, Multiscale porous Fe–N–C networks as highly efficient catalysts for the oxygen reduction reaction. *Nanoscale* 2019;11:19506-19511.
61. Liu W, Zhang L, Liu X, Liu X, Yang X, Miao S, Wang W, Wang A, and Zhang T, Discriminating Catalytically Active FeN_x Species of Atomically Dispersed Fe–N–C Catalyst for Selective Oxidation of the C–H Bond. *Journal of the American Chemical Society* 2017;139:10790-10798.
62. Peng Y, Bian Z, Zhang W, and Wang H, Identifying the key N species for electrocatalytic oxygen reduction reaction on N-doped graphene. *Nano Research* 2023;
63. Luo E, Xiao M, Ge J, Liu C, and Xing W, Selectively doping pyridinic and pyrrolic nitrogen into a 3D porous carbon matrix through template-induced edge engineering: enhanced catalytic activity towards the oxygen reduction reaction. *Journal of Materials Chemistry A* 2017;5:21709-21714.
64. Wang R, Zhang P, Wang Y, Wang Y, Zaghib K, and Zhou Z, ZIF-derived Co–N–C ORR catalyst with high performance in proton exchange membrane fuel cells. *Progress in Natural Science: Materials International* 2020;30:855-860.
65. Zhong G, Xu S, Liu L, Zheng CZ, Dou J, Wang F, Fu X, Liao W, and Wang H, Effect of Experimental Operations on the Limiting Current Density of Oxygen Reduction Reaction Evaluated by Rotating-Disk Electrode. *ChemElectroChem* 2020;7:1107-1114.
66. Huang Y, Liu W, Kan S, Liu P, Hao R, Hu H, Zhang J, Liu H, Liu M, and Liu K, Tuning morphology and structure of Fe–N–C catalyst for ultra-high oxygen reduction reaction activity. *International Journal of Hydrogen Energy* 2020;45:6380-6390.
67. Liu M, Lv X, Wang L, Chen K, Li Y, Sun T, Zhang J, Zhang L, and Sun S, Kinetically favorable edge-type iron–cobalt atomic pair sites synthesized via a silica xerogel approach for efficient bifunctional oxygen electrocatalysis. *Journal of Materials Chemistry A* 2023;11:708-716.
68. Asset T and Atanassov P, Iron-Nitrogen-Carbon Catalysts for Proton Exchange Membrane Fuel Cells. *Joule* 2020;4:33-44.
69. Shao C, Zhuang S, Zhang H, Jiang Q, Xu X, Ye J, Li B, and Wang X, Enhancement of Mass Transport for Oxygen Reduction Reaction Using Petal-Like Porous Fe-NC Nanosheet. *Small* 2021;17:2006178.

70. Speck FD, Santori PG, Jaouen F, and Cherevko S, Mechanisms of Manganese Oxide Electrocatalysts Degradation during Oxygen Reduction and Oxygen Evolution Reactions. *The Journal of Physical Chemistry C* 2019;123:25267-25277.
71. Vezzù K, Bach Delpeuch A, Negro E, Polizzi S, Nawn G, Bertasi F, Pagot G, Artyushkova K, Atanassov P, and Di Noto V, Fe-carbon nitride "Core-shell" electrocatalysts for the oxygen reduction reaction. *Electrochimica Acta* 2016;222:1778-1791.
72. Wei Q, Zhang G, Yang X, Fu Y, Yang G, Chen N, Chen W, and Sun S, Litchi-like porous Fe/N/C spheres with atomically dispersed FeN_x promoted by sulfur as highly efficient oxygen electrocatalysts for Zn–air batteries. *Journal of Materials Chemistry A* 2018;6:4605-4610.
73. Kumar K, Asset T, Li X, Liu Y, Yan X, Chen Y, Mermoux M, Pan X, Atanassov P, Maillard F, and Dubau L, Fe–N–C Electrocatalysts' Durability: Effects of Single Atoms' Mobility and Clustering. *ACS Catalysis* 2021;11:484-494.
74. Zhang Y, Huang L-B, Jiang W-J, Zhang X, Chen Y-Y, Wei Z, Wan L-J, and Hu J-S, Sodium chloride-assisted green synthesis of a 3D Fe–N–C hybrid as a highly active electrocatalyst for the oxygen reduction reaction. *Journal of Materials Chemistry A* 2016;4:7781-7787.
75. Wang L, Wan X, Liu S, Xu L, and Shui J, Fe-N-C catalysts for PEMFC: Progress towards the commercial application under DOE reference. *Journal of Energy Chemistry* 2019;39:77-87.
76. Shao Y, Dodelet J-P, Wu G, and Zelenay P, PGM-Free Cathode Catalysts for PEM Fuel Cells: A Mini-Review on Stability Challenges. *Advanced Materials* 2019;31:1807615.
77. Zhang J, Yuan Y, Gao L, Zeng G, Li M, and Huang H, Stabilizing Pt-Based Electrocatalysts for Oxygen Reduction Reaction: Fundamental Understanding and Design Strategies. *Advanced Materials* 2021;33:2006494.
78. Xu C, Chen L, Wen Y, Qin S, Li H, Hou Z, Huang Z, Zhou H, and Kuang Y, A co-operative protection strategy to synthesize highly active and durable Fe/N co–doped carbon towards oxygen reduction reaction in Zn–air batteries. *Materials Today Energy* 2021;21:100721.
79. Martinez U, Komini Babu S, Holby EF, and Zelenay P, Durability challenges and perspective in the development of PGM-free electrocatalysts for the oxygen reduction reaction. *Current Opinion in Electrochemistry* 2018;9:224-232.
80. Weiss J, Zhang H, and Zelenay P, Recent progress in the durability of Fe-N-C oxygen reduction electrocatalysts for polymer electrolyte fuel cells. *Journal of Electroanalytical Chemistry* 2020;875:114696.